Atom-interferometric studies of light scattering

S. Beattie,[1] B. Barrett,[1] I. Chan,[1] C. Mok,[1] I. Yavin,[2] and A. Kumarakrishnan[1]

[1]*Department of Physics and Astronomy, York University, Toronto, Ontario, Canada M3J 1P3*
[2]*Joseph Henry Laboratories, Princeton University, Princeton, New Jersey 08544, USA*

We have used an echo-type atom interferometer that manipulates laser-cooled atoms in a single ground state to investigate the effect of light scattering from pulsed and continuous-wave light. The interferometer uses two off-resonant standing-wave pulses applied at times $t=0$ and $t=T$ to diffract and recombine momentum states separated by $2\hbar k$ at $t=2T$. Matter wave interference is associated with the formation of a density grating with period $\lambda/2$ in the vicinity of this echo time. The grating contrast is measured by recording the intensity of coherently backscattered light. The interferometer is perturbed by an additional pulse applied at $t=2T-\delta T$ or by continuous-wave background light. If the additional pulse is a standing wave, the momentum states interfering at $t=2T$ are displaced and the grating contrast can be completely recovered due to constructive interference. In this case, the contrast shows a periodic modulation at the atomic recoil frequency as a function of δT. In a recent work, it was shown that the atomic recoil frequency can be measured easily and precisely when using coherence functions to model the signal shape. This paper provides an alternative description of the signal shape through an analytical calculation of echo formation in the presence of an additional standing-wave pulse. Using this treatment, it is possible to model the effects of spontaneous emission and spatial profile of the laser beam on the signal shape. Additionally, the theory predicts scaling laws as a function of the pulse area and the number of additional standing-wave pulses. These scaling laws are investigated experimentally and can be exploited to improve precision measurements of the atomic recoil frequency. We also show that coherence functions can be used to make a direct measurement of the populations of momentum states associated with the ground state under conditions where the Doppler-broadened velocity distribution of the sample is much larger than the recoil velocity. These measurements are consistent with Monte Carlo wave-function simulations. If the additional pulse is a traveling wave, we find that the grating contrast measured as a function of δT can be modeled by a quasiperiodic coherence function as in previous experiments that utilized atomic beams. In this work, we investigate the dependence of the photon scattering rate on the intensity and detuning of the traveling wave. We also study the effects of perturbing the interferometer with continuous-wave light and find that the dependence of the photon scattering rate on the intensity and detuning of the perturbing field is consistent with expectations.

I. INTRODUCTION

There has been considerable interest in using atom interferometers (AIs) that utilize laser-cooled samples to obtain high-precision measurements of the atomic fine structure constant, α [1–4]. Whereas the work in Refs. [1,2] relied on Raman transitions between hyperfine ground states in cesium, several experiments have used single state AIs in which Rb atoms are manipulated in a single ground state [5–11]. The first demonstration of a single state AI [5] used echo techniques to observe the effects of atomic recoil. This AI uses two off-resonant standing-wave pulses applied at $t=0$ and $t=T$ to diffract and recombine momentum states associated with the same internal atomic state. Atoms absorb momenta in units $2n\hbar k$ due to absorption and stimulated emission of photons from the traveling-wave components of the standing wave. Here, k is the wave vector of the traveling wave and n is an integer associated with the number of two-photon transitions. These momentum states represent different center-of-mass wave packets that accumulate a phase of $n^2\omega_r t$, where $\omega_r=\hbar\Delta k^2/2m$ is the atomic recoil frequency. Here, m is the atomic mass and $\Delta k=2\hbar k$ is the momentum transferred to atoms by the standing-wave pulse. The Doppler phases of these wave packets evolve as $n\Delta k v_0 t$, where

v_0 is the initial atomic velocity. For a sufficiently cold sample, the temporal phase modulation of the atomic wave function at ω_r can be detected if the characteristic Doppler dephasing time $\tau_D \sim 1/ku > T_r$ [6]. Here $T_r=\pi/\omega_r \sim 32$ μs is the recoil period and u is the most probable speed of the atomic sample. For a laser-cooled sample at a temperature of 50 μK, as in this work, $\tau_D \sim 1$ μs $\ll T_r$. In this case, the effects of atomic recoil can be observed using the echo technique. Therefore, an echo-type AI offers a general technique to cancel the effect of the velocity distribution and observe recoil oscillations even if the velocity distribution of the sample is much larger than the recoil velocity, $v_r=\hbar k/m$. Such an AI avoids the necessity of velocity selection.

The momentum states associated with each atom can be recombined by the second standing wave on a time scale that should be limited only by the transit time, τ_T, of cold atoms through the region of interaction defined by the laser beams. Typically, $\tau_T \sim 100$ ms so that the separation between wave packets representing momentum states shown in Fig. 1(a) can be much larger than the de Broglie wavelength. Interference of momentum states after interaction with the two standing-wave pulses occurs in the vicinity of echo times $t=2T, 3T$, etc. The interference is associated with the formation of density gratings with spatial modulations at subharmonics of $\lambda/2$ [5,12]. Here, λ is the wavelength of light. In
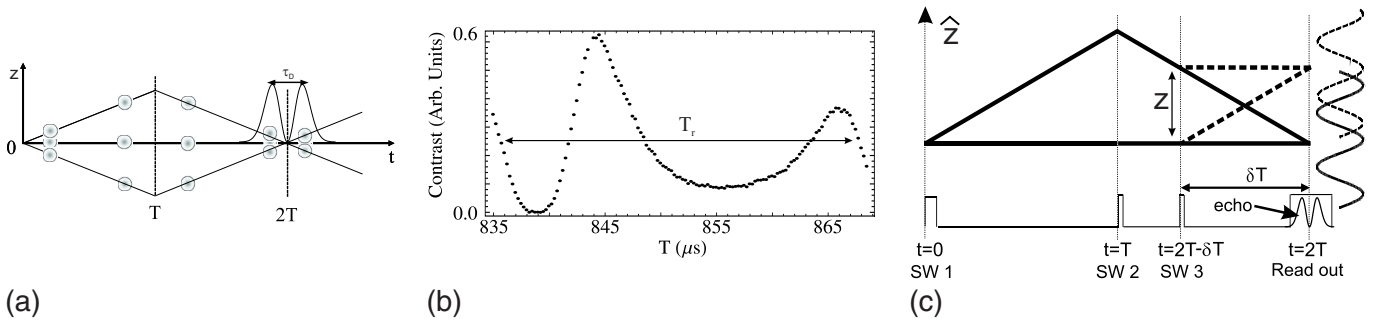
FIG. 1. (Color online) (a) Billiard ball representation of momentum state interference in the echo experiment. The figure shows only the 0 and $\pm 2\hbar k$ momentum states. The characteristic echo envelope near $t=2T$ has a duration τ_D due to Doppler dephasing. (b) Echo amplitude versus T obtained by integrating the echo envelope shown in (a). The signal has a period T_r. (c) Effect of an additional pulse (SW3) on the AI. Two interfering momentum states (solid black lines) are perturbed by an additional standing-wave pulse applied at $t=2T-\delta T$. This pulse can affect both arms of the interferometer resulting in interference between displaced trajectories (dashed lines) that is phase shifted with respect to the original interference pattern. Constructive interference is observed if δT is an integer multiple of T_r.

this work, we focus exclusively on the grating with period $\lambda/2$ that forms in the vicinity of $t=2T$. The contrast of this grating can be detected by coherently backscattering a traveling-wave readout pulse. The backscattered signal is known as an echo and has a characteristic envelope that is shown in Fig. 1(a). The signal envelope represents the effect of averaging over the velocity distribution of the sample. The echo amplitude exhibits a modulation as a function of T that is periodic at ω_r. The modulation period, T_r, shown in Fig. 1(b), is the characteristic time in which a momentum kick of $2\hbar k$ causes a displacement of wave packets through a distance $\lambda/2$.

The Talbot time $T_{\text{Talbot}}=2T_r$ defines the time scale on which recoil effects become significant [13]. The Talbot effect refers to the repeated self-imaging of a diffraction grating from a collimated source first observed in classical optics [14]. A number of experiments in atom optics have used Talbot-Lau interferometers [15] in which there are strong overlap between diffracted atomic waves. In particular, effects of multiple phase gratings [16] and atomic diffraction in the Bragg regime [17–19] have been studied using atomic beams. The single-state AI used in this work is also a Talbot-Lau interferometer in which an "uncollimated" atomic cloud with a velocity spread much greater than v_r is diffracted by a standing wave pulse. A second standing wave is used to cancel the Doppler phases of wave packets so that grating formation occurs at echo times. Interesting applications of this interferometer include techniques for imaging nanostructures [20].

Previous work using this echo-type AI and dilute samples of laser-cooled atoms [5,7,9,10], have demonstrated that a precise measurement of α can be related to a measurement of $\hbar/m$ obtained by measuring T_r over a long time scale. The work in Refs. [5,7] describes preliminary measurements in the time domain and frequency domain, respectively. Reference [8] discusses the effects of magnetic field gradients and gravitational acceleration on time domain measurements. A more complete analysis of the challenges of extracting T_r due to changes in the signal shape caused by the effect of spontaneous emission and spatial intensity profile of the excitation beams is presented in Ref. [10]. The techniques described in Ref. [10] were used in Ref. [9] to measure ω_r to a

precision of ~ 2.6 parts per million (ppm). This result was obtained by averaging the results of 80 data sets and showed that the AI has reduced sensitivity to systematic effects such as the ac Stark shifts and magnetic fields. Other advantages of using dilute cold-atom samples for these measurements are that systematic effects due to interatomic interactions and the refractive index of the cloud observed in Bose-Einstein condensates (BECs) [6,21] can be avoided or reduced significantly.

In this paper, we describe several aspects of a recently developed technique that allows ω_r to be measured easily and precisely [11]. The technique relies on the influence of an additional pulse applied at $t=2T-\delta T$ during the AI pulse sequence as shown in Fig. 1(c). If the additional pulse is a standing wave, it interacts with all interfering pairs of momentum states and creates displaced trajectories that will interfere at $t=2T$ with a phase shift with respect to the original trajectories as shown in Fig. 1(c). The grating contrast, measured as a function of δT, shows periodic revivals if δT is an integer multiple of T_r. The revival of the contrast can be used to measure ω_r with high precision by carrying out the experiment over a suitably long time scale. The signal shape was modeled using coherence functions associated with standing-wave excitation. The use of these functions allows the grating contrast to be accurately described without a detailed knowledge of effects such as spontaneous emission and spatial profile [10]. Therefore the fits used to extract ω_r are extremely simple and robust.

Coherence functions for traveling-wave excitation were previously used to describe the results of atomic beam experiments [22–25]. These functions, which were calculated in Ref. [26], are the Fourier transforms of the atomic momentum distributions associated with the excitation pulse. In atomic beam experiments, the interaction time of the atoms in the excitation zones is determined by the longitudinal velocity distribution. In comparison, the work in Ref. [11] and in this paper describes the effect of temporally separated pulses that interact with all atoms in a cold sample for the same duration. The main advantage of a time domain experiment is that the pulse timing can be controlled easily and accurately.

An important result of this paper is an analytical calculation of the modulated grating contrast observed in Ref. [11].

This calculation is based on the theory of echo formation described in Ref. [12]. There are two major advantages of using the theory of echo formation. First, the formalism predicts the contributions to the signal shape due to spontaneous emission and spatial profile effects based on the treatment in [10]. Second, the theory predicts scaling laws for the contrast as a function of the number and area of the additional standing-wave pulses. In this paper, we also present an experimental investigation of these scaling laws.

Another significant result of this paper is a direct measurement of momentum state populations in the presence of spontaneous emission and spatial profile effects. The populations were varied by adjusting the pulse area of the additional pulse. We confirm the accuracy of the measurements using Monte Carlo wave-function simulations.

We also present an experimental investigation of the effect of an additional traveling-wave pulse applied at $t = 2T - \delta T$. In this case, the grating contrast also exhibits revivals that are modulated at $\sim \omega_r$. However, there is a loss in contrast due to decoherence associated with spontaneous emission. The signal shape can be modeled by a quasiperiodic coherence function. This aspect of our work shows the strong connection to previous studies in atomic beams [22–25]. As in beam experiments, it is possible to extract the probabilities of single and multiple photon scattering events from the data. In addition, we present a measurement of the photon scattering rate as a function of detuning and pulse intensity.

Finally, we investigate the behavior of the grating contrast in the presence of continuous-wave (cw) light and measure scaling laws for the photon scattering rate. A related aspect involving a measurement of the photon cross section is presented in [11].

These experiments assume significance in the context of several recent studies in ultracold samples. The work presented in Ref. [27] initiated studies of quantum chaos using a δ-kicked rotor. Reference [28] described predictions for the preservation of contrast following a large number of excitation pulses. Observations of higher-order quantum resonances at fractional multiples of T_r in BEC and numerical simulations are presented in recent work [29,30]. The work in Ref. [31] used microwave echo spectroscopy for investigations of contrast in both quantum and classical regimes, whereas the work described in [32,33] used the echo-type interferometer described in this paper to investigate the preservation of contrast following excitation by a large number of standing-wave pulses separated by T_r. These authors have also proposed a precision measurement of ω_r. Other experiments that have investigated quantum resonances include Refs. [34,35]. In these papers, the authors demonstrate the ability to transfer a large number of recoil momenta to cold atoms using multiple standing-wave pulses that satisfy the criteria for a quantum resonance.

This paper is outlined as follows: in Sec. II, we present a brief summary of the theory of coherence functions. Subsequently, we present the theory of echo formation to describe the effect of an additional standing-wave pulse and discuss scaling laws. Section III presents an overview of the experiment, and Sec. IV discusses the results that involve the distinctive effects of standing-wave, traveling-wave, and cw light on the echo-type AI.

II. THEORY

A. Coherence function theory

Although photon scattering can destroy the coherence between momentum states of the AI, the coherence can be preserved if which-path information is not obtained from the scattered photons. This aspect has been extensively examined using the conceptual framework of the Heisenberg microscope [36] in both classical optics and atom optics [23,25]. In the rest frame of monoenergetic atoms, the effect of spatially separated laser fields is equivalent to the effect of temporally separated pulses acting on a localized sample of cold atoms. Therefore, the results used to describe atomic beam experiments can easily be applied to the time domain experiments described in this work.

We now provide a brief discussion of the theory of coherence functions. These functions can be used to model the effects of an additional pulse, which can be either a traveling wave or a standing wave. In the presence of a third pulse, the coherence function can be expressed as the correlation between interfering states separated by displacement, z, as shown in Fig. 1(c). This can be written as

$$g(z) = \int \phi(z' - z)\phi^*(z')dz' = \mathcal{F}_z\{I(k)\}, \quad (1)$$

where $\phi(z)$ is the atomic wave function and $\mathcal{F}_z$ represents a Fourier transform of the momentum distribution of the atoms caused by the third pulse, $I(k)$.

The momentum distribution depends on pulse parameters such as polarization, duration, intensity, and detuning. For the case of a circularly polarized traveling-wave pulse propagating along the z axis, it can be shown that the momentum distribution (along $\hat{z}$) associated with a single spontaneous emission event is given by

$$I(k) = \frac{3}{8k_p}\left[1 + \frac{k^2}{k_p^2}\right]. \quad (2)$$

This distribution ranges from $-k_p < k < k_p$, where k_p is the $\hat{z}$ component of the wave vector of photons in the third pulse. The signal shape is associated with the radiation pattern of a dipole oscillating in the x-y plane. Due to the momentum kick from the initial absorption, the atomic momentum distribution after a photon is scattered is given by $I(k - k_p)$. This is shown in Fig. 2(a). The corresponding coherence function is given by

$$g_1(z) = \frac{3e^{ik_p z}\{zk_p \cos(zk_p) + [(k_p z)^2 - 1]\sin(k_p z)\}}{2(k_p z)^3}, \quad (3)$$

where the spatial variable z is in units of the optical wavelength, λ, and the subscript 1 denotes that this coherence function describes a single photon scattering event. The modulus of this function is shown in Fig. 2(b). It is the Fourier transform of Eq. (2) and resembles the diffraction pattern of a single slit. The overall loss in contrast in the interferometer is due to decoherence from spontaneous emission events. In the presence of multiple-photon scattering events, the convolution theorem can be used to show that the
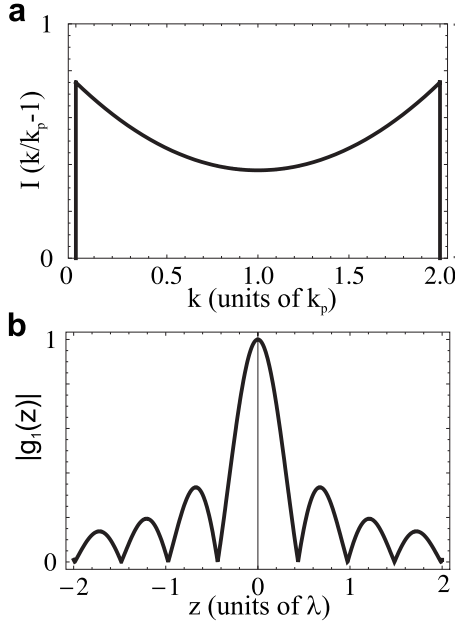
FIG. 2. (a) Momentum distribution, $I(k/k_p-1)$, after absorption and spontaneous emission of a single photon from traveling-wave excitation. k_p is the $\hat{z}$ component of the photon k vector. (b) Coherence function (in units of the optical wavelength, λ) that represents the grating contrast corresponding to $I(k/k_p-1)$ shown in (a).

FIG. 3. (a) Momentum distribution, $I(k/k_p)$, modeled for standing-wave excitation where $\Delta=40$ MHz, $\tau_p=86$ ns, and intensity $\sim 5I_{\text{sat}}$. (b) Coherence function that represents the grating contrast corresponding to $I(k/k_p)$ shown in (a).

coherence functions for n photon scattering events is $g_1^n(z)$. The final coherence function can be written as

$$g(z) = \sum_{n=0}^{\infty} c_n g_1^n(z), \qquad (4)$$

where c_n are weighting coefficients that give the probabilities of populating the $2n\hbar$ momentum state.

For the case of a standing-wave third pulse, the shape of the coherence function is notably different and resembles a multislit interference pattern. Since the traveling-wave components of the pulse are far-detuned two-photon processes will dominate and spontaneous emission can be neglected. Therefore, atoms will receive momentum kicks in integer multiples of $2\hbar k_p$ and the momentum distribution associated with the third pulse will resemble a series of δ functions separated by $2k_p$ as shown in Fig. 3(a). The relative amplitudes of the peaks represent probabilities of momentum states and the range can be limited by the pulse bandwidth.

The associated coherence function is shown in Fig. 3(b) and is given by

$$g(z) = \sum_{n=0}^{\infty} c_n e^{\pm i2nk_pz}. \qquad (5)$$

This function shows that the contrast can be completely regained when $k_pz=\pi$. This feature was exploited in Ref. [11] to make a measurement of ω_r precise to 1.6 ppm. Since the AI used in this work operates in the time domain with a cloud of trapped atoms, we will describe the results in terms of the coherence function $g(\delta T)$. In this case, $\delta T=\frac{mz}{\hbar\Delta k}$, where z is the spatial separation between arms of the interferometer
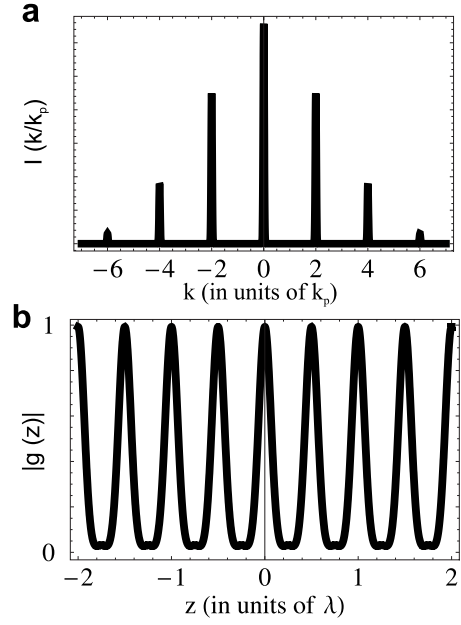
and δT is the time delay between the additional pulse and the echo time.

B. Calculation of echo formation for multiple pulses

The theory of echo formation provides an alternative theoretical framework for understanding the effect of additional standing-wave pulses applied during the AI pulse sequence. We consider the following pulse sequence:

$$\text{first AI echo pulse} \quad t=0$$

$$\text{second AI echo pulse} \quad t=T$$

$$\text{first perturbation pulse} \quad t=2T-\delta T-(N-1)T_r$$

$$\text{second perturbation pulse} \quad t=2T-\delta T-(N-2)T_r$$

$$\vdots \qquad \vdots$$

$$N\text{th perturbation pulse} \quad t=2T-\delta T. \qquad (6)$$

Here, all standing-wave pulses produce similar potentials and therefore interact with atoms in a similar manner. The first two standing-wave pulses produce momentum state interference at the echo time, $t=2T$, at which the signal is detected. For all experiments, we keep T fixed and observe the effect of additional pulses on the contrast at $t=2T$. Therefore, for clarity and in order to facilitate the comparison with experimental results, we will refer to the first two pulses as AI echo pulses and any additional standing-wave pulses as "perturbation" pulses.

For the specific case in which the standing-wave potential is strictly periodic [5,10], the expression for the Δk compo-

nent of the atomic density distribution following interaction with multiple pulses can be derived on the basis of Eqs. (11)–(14) of Ref. [12]. After some lengthy but straightforward algebra, it can be shown that the Δk component after all excitation pulses is given by

$$\rho(\vec{x},t) = \sum_{m_L=-\infty}^{\infty} \rho_{m_L}(t) e^{im_L \overrightarrow{\Delta k} \cdot \vec{x}}, \tag{7}$$

where $L=N+2$ is the total number of standing-wave pulses and m_L is an index running over all the Fourier harmonics that result from the interference of partial waves that differ in momenta by $m_L \hbar \Delta k$. Here, $\overrightarrow{\Delta k} = \vec{k}_1 - \vec{k}_2$ is the difference between wave vectors of the traveling-wave components of the standing wave. Each harmonic has an associated atomic density given by $\rho_{m_L}(t)$.

The readout pulse at $t=2T$ is sensitive to the fundamental harmonics ($m_L = \pm 1$) that represents the grating contrast measured in the experiment. The atomic density at $t=t^{\text{echo}} + t'$ is given by

$$\rho_{m_L}(t') = \sum_{m_1 \cdots m_{(L-1)}=-\infty}^{\infty} \langle e^{-(\Delta k v_0 t'/2)^2} \rangle$$
$$\times \prod_{j=1}^{L} J_{m_j - m_{(j-1)}} \{ 2\phi_j \sin[\varphi_j(t^{\text{echo}} + t')] \}, \tag{8}$$

where $\langle \cdots \rangle$ represents the average over the initial velocity distribution, t' is the time with respect to $2T$, $J_{m_j - m_{(j-1)}}$ is a Bessel function of the first kind and order $m_j - m_{(j-1)}$, and φ_j are phases that will be defined for specific cases. As shown in Fig. 1(a) the echo signal is observed for a time $t' \sim \tau_D$ due to Doppler dephasing. The pulse areas ϕ_j are defined as

$$\phi_j = \frac{\Omega^2}{8\Delta} \left(1 - i\frac{\Gamma}{\Delta} \right) \tau_j \equiv |\phi_j| e^{i\theta}, \tag{9}$$

where Ω is the single photon Rabi frequency, Δ is the detuning, Γ is the effective decay rate of the excited state, τ_j is the pulse duration, and $\theta = \tan^{-1}(-\Gamma/\Delta)$ is a parameter that quantifies spontaneous emission during the excitation. In Eqs. (8) and (9) we first assume $\Delta \gg \Gamma$ and neglect the effect of spontaneous emission, i.e., $\theta = 0$. The echo times are given by

$$t^{\text{echo}} = \left(2 - \frac{m_1 + m_2}{m_L} \right) T + \left(\frac{m_2 - m_L}{m_L} \right) \delta T$$
$$+ \frac{1}{m_L} \left[(N-1)m_2 - \sum_{j=3}^{L-1} m_j \right] T_r. \tag{10}$$

Therefore, in order to have an echo at $t=2T$ we require

$$m_1 + m_2 = 0, \tag{11}$$

$$m_2 - m_L = 0, \tag{12}$$

and

$$Nm_2 - \sum_{j=3}^{L} m_j = 0. \tag{13}$$

With these conditions imposed, the phases φ_j in Eq. (8) for $j=3,\ldots,L$ are simplified and at $t=t^{\text{echo}} + t'$ are given by

$$\varphi_1 = \omega_r m_L t',$$

$$\varphi_2 = \omega_r(m_L t' - m_1 T),$$

$$\varphi_j = \omega_r \left[m_L(t' + \delta T) + T_r \sum_{k=j}^{L-1} m_k \right] \quad j=3,\ldots,L. \tag{14}$$

To achieve more accurate fits to the data, the effects of spontaneous emission must be included as in Ref. [10]. The resulting expression for the Δk component of the atomic density is

$$\rho_1(t) = \sum_{m_1 \ldots m_{(L-1)}=-\infty}^{\infty} \langle e^{-(\Delta k v_0 t'/2)^2} \rangle$$
$$\times \prod_{j=1}^{L} J_{m_j - m_{(j-1)}}(\bar{\omega}_j) \left(\frac{\sin(\varphi_j - \theta)}{\sin(\varphi_j + \theta)} \right)^{m_j - m_{(j-1)}}, \tag{15}$$

where

$$\bar{\omega}_j = 2|\phi_j| \sqrt{\sin(\varphi_j - \theta)\sin(\varphi_j + \theta)}. \tag{16}$$

Equations (15) and (16) describe the echo signal with N additional pulses. We now consider some special cases where a simple expression for the signal shape can be obtained.

C. Single perturbation pulse

To obtain the echo signal in the presence of a single standing-wave perturbation pulse, we use $N=1$ in Eq. (13). Since $m_L = m_3 = 1$, we use Eqs. (11)–(13) to obtain

$$m_2 = 1 \quad \text{and} \quad m_1 = -1. \tag{17}$$

As a result, the Δk component of the atomic density is given by

$$\rho_1 \propto J_1[2\phi_1 \sin(\omega_r t')] J_2\{2\phi_2 \sin[\omega_r(t'+T)]\}$$
$$\times J_0\{2\phi \sin[\omega_r(t'+\delta T)]\}, \tag{18}$$

where ϕ_1, ϕ_2 are the pulse areas of the first and second AI pulses respectively, and ϕ is the area of the perturbation pulse. We note that the Boltzmann averaging factor is omitted. If $t' \ll \delta T$, the Δk component of the atomic density at the time of the echo is a function of δT given by

$$\rho_1 \propto J_0[2\phi \sin(\omega_r \delta T)]. \tag{19}$$

This is a symmetric function with period π/ω_r. This signal shape resembles the periodic grating contrast predicted by coherence functions and shown in Fig. 3(b). The full width at half maxima (FWHM) of the periodic revivals of this function depends on the pulse area as shown in Fig. 4. Expanding about $\delta T=0$ we obtain
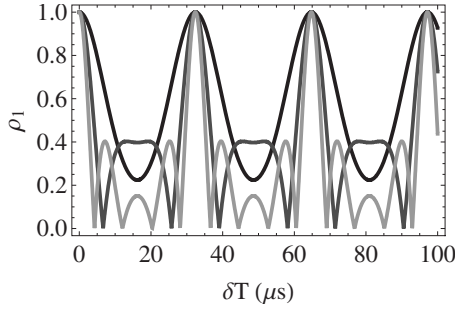
FIG. 4. Plots of $|\rho_1|$ from Eq. (19) for various pulse areas; ϕ =1 for the black curve, ϕ=2 for the dark gray curve, and ϕ=3 for the light gray curve. The FWHM of the revivals in $|\rho_1|$ decreases as ϕ is increased. The additional zeroes in the signal are not observed experimentally since the effects of spontaneous emission and spatial profile cause a smoothing of the signal.

$$\text{FWHM} \approx \frac{\sqrt{2}}{\omega_r \phi}. \tag{20}$$

In Ref. [11], the grating contrast with a single standing-wave perturbation pulse was recorded over the time scale of the experiment to obtain a precision measurement of ω_r. The precision is improved by decreasing the fringe width. This can be achieved by increasing the area of the perturbation pulse ϕ as predicted by Eq. (20).

Fringe narrowing has previously been observed in an internal state-labeled interferometer that used dark states [37]. In this work, interference between multiple paths resulted in a narrowing of the fringes. This is analogous to the narrowing of interference fringes due to the interference of higher-order momentum states discussed in this work.

If spontaneous emission is included in the theory, the dependence on δT is more complicated. Using Eqs. (15) and (16) we obtain

$$\rho_1 \propto J_0[2|\phi|\sqrt{\sin(\omega_r \delta T + \theta)\sin(\omega_r \delta T - \theta)}]. \tag{21}$$

To describe the signal shape with greater accuracy, the spatial profile of the laser field must be taken into account since the pulse area varies across the atomic sample. It can be shown based on Ref. [9] that the effect of the spatial profile is given by integrating the Bessel function in Eq. (21) over the spatial coordinate x as given by

$$\rho_1 \propto \int_0^1 dx J_0(a_0 x) J_1(a_1 x) J_2(a_2 x). \tag{22}$$

Here, a_i are the arguments of the Bessel functions in Eq. (18) modified to include spontaneous emission. The integral in Eq. (22) cannot be evaluated analytically. To fit to the data, a numerical evaluation is performed. In this paper, we will compare the signal shapes that follow from this theoretical treatment with the shapes predicted by coherence functions.

D. N perturbation pulses

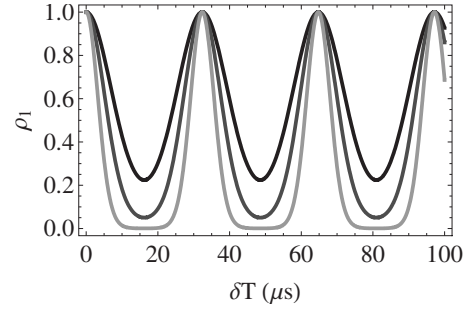We now discuss the reduction in FWHM as a function of the number of perturbation pulses. For the case of N addi-

FIG. 5. Plots of $|\rho_1|$ using Eq. (24) for various numbers of perturbation pulses; N=1 for the black curve, N=2 for the dark gray curve, and N=5 for the light gray curve. The FWHM of the revivals in ρ_1 decrease as N is increased. For all curves, ϕ=1.

tional standing-wave perturbation pulses, ρ_1 involves multiple sums over a large number of indices, m_j that are generally difficult to simplify. However, it is possible to simplify the expression if we are interested in the behavior near the maxima at $\delta T \approx l T_r$, where l is an integer. Because $\omega_r t' \ll 1$ and since $\sin(\omega_r \delta T) \approx 0$ near the maxima, ρ_1 is dominated by the term corresponding to

$$m_1 = -1, \quad m_2 = m_3 = \cdots = m_L = 1. \tag{23}$$

In this case,

$$\rho_1(t) \propto J_1[2\phi_1 \sin(\omega_r t')] J_2[2\phi_2 \sin(\omega_r T)]$$
$$\times \{J_0[2\phi \sin(\omega_r \delta T)]\}^N, \tag{24}$$

where we used $\sin[\omega_r(\delta T + l T_r)] = (-1)^l \sin(\omega_r \delta T)$ and the symmetry of $J_0(x)$. Figure 5 shows the reduction in FWHM that can be obtained by increasing the number of perturbation pulses. To investigate the scaling law that describes the FWHM as a function of N, we expand the Bessel function about zero and keep only the leading terms in N so that,

$$\{J_0[2\phi \sin(\omega_r \delta T)]\}^N \approx 1 - N\phi^2 \omega_r^2 \delta T^2. \tag{25}$$

Therefore, the decrease in FWHM with the number of pulses is given by

$$\text{FWHM} \sim \frac{1}{\omega_r \phi N^{1/2}}. \tag{26}$$

This result suggests that the precision associated with ω_r, which is proportional to the fringe width, should increase as $N^{1/2}$. In the experiment, we use a burst of N identical perturbation pulses separated by the calculated value of T_r and measure the grating contrast by varying the start time of the burst defined as $t = 2T - \delta T - (N-1)T_r$ in Eq. (6). Thus the time scale of the experiment is defined by the extent over which δT can be varied.

Reference [32] considers the use of a large number of perturbation pulses with $\phi \ll 1$ for a measurement of ω_r. In the technique proposed in Ref. [32], N is fixed and the pulse frequency is varied to map out the recoil resonance. We note that this method requires further explanation since some subtleties are involved. Prior knowledge of the position of the maxima in contrast ($\delta T \approx l T_r$) is required to define the reference time from which all pulses are delayed. This refer-

ence time can be determined by measuring the grating contrast as a function of δT at a fixed pulse frequency ($\approx \omega_r / \pi$). Therefore, a precision measurement using multiple perturbation pulses would require an iterative procedure in which the reference time and the pulse frequency are sequentially measured. For the technique described in Ref. [32] the time scale increases linearly with the number of perturbation pulses. Therefore, the prediction of Eq. (26) and the prediction in Ref. [32] that the FWHM scales as $N^{-3/2}$ are equivalent since a factor of N^{-1} in Ref. [32] is related to the linear increase in time scale with an increase in N.

In summary, the basic properties of the echo signal have been derived in response to single and multiple standing-wave perturbation pulses. Scaling laws for the improvement in precision with the pulse area, ϕ, and the number of pulses, N, have been discussed.

III. EXPERIMENT

The light used for atom trapping and atom interferometry is derived from a Ti:sapphire ring laser and from a semiconductor tapered amplifier seeded by light from the Ti:sapphire laser. Approximately 10^8 ^{85}Rb atoms are loaded into a magneto-optical trap (MOT) on a time scale of ~ 100 ms using fiber-coupled trapping laser beams with a beam diameter of ~ 3.5 cm. The trapping laser is tuned $\sim 2\Gamma_N$ below resonance during the loading phase where Γ_N is the natural linewidth of the $5S_{1/2}$ $F=3 \rightarrow 5P_{3/2}$ $F=4$ cycling transition. After turning off the MOT gradient coils in ~ 100 μs, the laser is frequency shifted to $\sim 5\Gamma_N$ below resonance for ~ 5 ms to further cool the atoms in a molasses. The temperature of the sample is inferred by photographing the ballistic expansion of the cloud using a charge-coupled device (CCD) camera and is typically ~ 50 μK [38]. The repump laser, which is resonant with the $5S_{1/2}$ $F=2 \rightarrow 5P_{3/2}$ $F=3$ transition, is derived from a grating-stabilized diode laser and is coupled through the same fiber as the trapping laser.

The excitation pulses for the AI are derived from a chain of acousto-optic modulators (AOMs) controlled by transistor-transistor logic (TTL) switches that ensure an extinction ratio for the radio frequency (RF) power of ~ 40 dB. Pulsing a chain of AOMs ensures that excitation and readout pulse have on/off contrast greater than 10^6:1, thereby minimizing decoherence due to background light. The last AOM in this chain operates at 250 MHz and is shown in Fig. 6(a). The diffracted beam from this AOM serves as the excitation beam. The diameter of this beam is ~ 1 cm which is larger than the initial cloud diameter of ~ 4 mm. The mirror shown at the top of Fig. 6(a) is used to retroreflect the traveling-wave pulses from the AOM and produce the two standing-wave excitation pulses used for the AI and the standing-wave perturbation pulses. A shutter with a closing time of ~ 600 μs is used to block the retroreflection at the time of the readout pulse. With the shutter closed, it is also possible to perturb the AI with traveling wave pulses.

The grating contrast is detected using a readout pulse that has the same detuning as the excitation pulses. The backscattered light from the sample due to the readout pulse is detected using a gated photomultiplier tube (PMT). The PMT
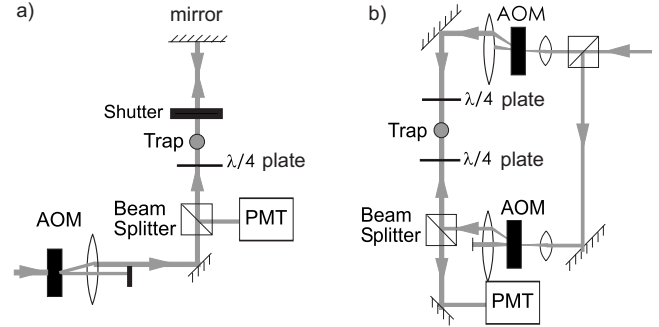

FIG. 6. (a) Experimental setup using a single retro-reflected beam. (b) Experimental setup using two separate, counterpropagating beams.

has a rise time of ~ 10 ns and the gate can be fully opened on a time scale of 100 ns. Due to jitter in the shutter closing time of ~ 200 μs, the smallest pulse separations, T, for which the echo can be recorded using this technique is ~ 1 ms. The backscattered signal is typically averaged over 32 repetitions and the grating contrast is determined by integrating the echo envelope over the signal duration of ~ 2 μs. The signal is normalized by dividing by the amplitude obtained in the absence of a perturbation pulse.

The peak intensities of all AI pulses is $I \sim 5 - 10$ I_{sat}, where $I_{sat} = 7.56$ mW/cm^2 is the saturation intensity calculated assuming equally populated magnetic sublevels of the ^{85}Rb ground state. The durations of the of the first and second AI pulses are 500–800 ns and 40–200 ns, respectively. For studies of light scattering with standing-wave and traveling-wave perturbation pulses, the pulse durations are $\sim 40 - 300$ ns. The timing of all pulses is controlled by digital delay generators. The time base of these generators is slaved to a Rb atomic clock with an Allan variance of 2 $\times 10^{-12}$ at 100 s. The 250 MHz oscillator controlling the AOM is also phase locked to the clock. In this arrangement, the delays between pulses are precise to 500 ps.

For some experiments, two separate AOMs operating at 250 MHz were used to generate counterpropagating traveling-wave pulses as shown in Fig. 6(b). These pulses were spatially overlapped to generate standing-wave pulses. The beam diameters of the excitation beams were ~ 6 mm in this case. This arrangement allowed the shutter to be eliminated so that the time separation between the standing-wave excitation pulses, T, could be reduced to a few microseconds.

IV. RESULTS

A. Scaling laws for grating contrast

We will now discuss measurements of scaling laws associated with the FWHM of the revivals in contrast as a function of pulse area ϕ. The theoretical predictions for the signal shape in the presence of a single standing-wave perturbation pulse are shown in Fig. 4. The inset in Fig. 7 shows the grating contrast as a function of δT. The time between AI echo pulses is fixed at $T \sim 1.6$ ms. The AI pulses and the perturbation pulse have the same intensity and detuning. Each curve in the inset was obtained for a specific perturba-
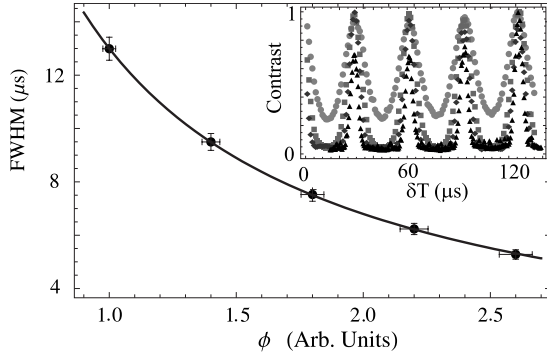
FIG. 7. Inset shows the grating contrast as a function of δT. $\tau_p=50$ ns (circles), 70 ns (squares), 90 ns (diamonds), and 130 ns (triangles). Body of figure shows FWHM of the peaks in inset as a function of perturbation pulse area (varied by changing τ_p). The data are fit to the form $A\phi_p^{-p}$ giving $A=13.00\pm0.03$ μs and $p=0.95\pm0.1$, which is consistent with the predictions of Eq. (20)

tion pulse duration, τ_p. The data shows that the contrast can be completely regained if $\delta T = l T_r$. The periodic revivals are due to constructive interference between displaced trajectories shown in Fig. 1(c). It is obvious that the data are qualitatively similar to the coherence function shown in Fig. 3(b). Therefore, the data can be fit using Eq. (5) where terms up to $n=5$ are included in the fitting functions. The coefficients c_n are associated with the relative amplitudes of the peaks in Fig. 3(a) and represent the probabilities of the atom acquiring momenta in units of $2n\hbar k$ during the perturbation pulse. As τ_p is increased, thereby increasing ϕ, the FWHM of the curves decreases monotonically and the fit parameters associated with $g(\delta T)$ show that higher-order momentum states contribute to the signal. The body of Fig. 7 shows the variation in the FWHM for the curves in the inset as a function of τ_p. A fit to this data shows that the FWHM scales as $1/\tau_p$ which is consistent with the predicted dependence on ϕ given by Eq. (20).

We now present a study of the dependence of the FWHM on the number of standing-wave perturbation pulses. This effect was discussed in Sec. II D. Figure 8 shows the FWHM as a function of the number of perturbation pulses, N. The durations of all these pulses were fixed at $\tau_p=40$ ns. Under
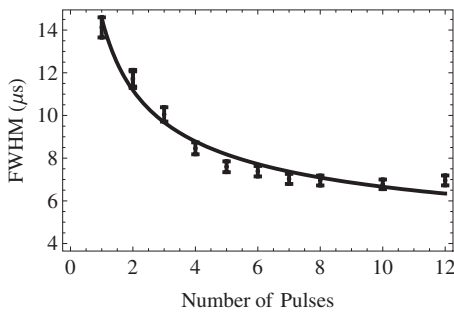

FIG. 8. FWHM of the revivals in grating contrast as a function of the number of standing-wave perturbation pulses, N. The perturbation pulses are identical and are separated by T_r, with $\tau_p=40$ ns and $\Delta=40$ MHz. The solid line is fit to the data using the function FWHM$=a+b\times N^{-1/2}$. The fit yields values $a=3\pm0.4$ and $b=11.6\pm0.7$.
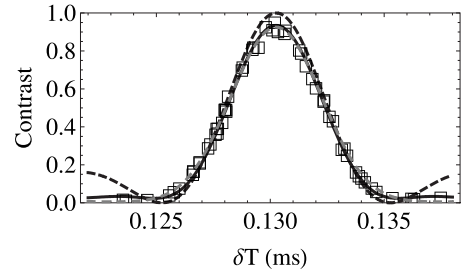

FIG. 9. Dashed curve shows a fit to the data using Eq. (19), neglecting the effects of spontaneous emission and the spatial profile of the laser beam. The gray curve shows a fit based on Eqs. (21) and (22) that includes the effects of spontaneous emission and spatial profile. The black curve shows a fit based on Eq. (5) that includes six Fourier coefficients that represent the probabilities of momentum states.

these conditions, the perturbation pulse area, ϕ, is of order unity. The pulses were separated by T_r (calculated from the definition). The data shows that the FWHM decreases with pulse number until it reaches a constant value for $N \sim 7$. We attribute the leveling off to the limited spectral bandwidth of the perturbation pulses, which limits the range of momentum states that these pulses can address. Equation (26) predicts that the FWHM should scale as $1/N^{1/2}$. However, the data deviates from this predicted dependence at high values of N, as shown in Fig. 8. Nevertheless, separate data with increased perturbation pulse bandwidth exhibited a monotonic decrease in the FWHM up to a larger value of N, which is qualitatively consistent with expectations.

B. Fits to signal shape

We now discuss the functional form of the revivals in grating contrast using the theory of echo formation presented in Sec. II C and the theory of coherence functions presented in Sec. II A. Figure 9 shows fits to a single revival in the inset in Fig. 7 based on both theoretical treatments. The dashed black line is a fit based on Eq. (19) that neglects the effects of spontaneous emission and spatial profiles of the trapped sample and the excitation laser beams. The solid black line shows a fit that includes both these effects based on Eqs. (21) and (22). It is evident that the accuracy of the fits improves tremendously when these effects are taken into account.

The dashed gray line in Fig. 9 is a fit based on Eq. (5) that was used in Ref. [11] for a precise measurement of ω_r. Although both theoretical treatments produce accurate fits, the technique based on coherence functions results in more robust fits. This is because the effects of spontaneous emission and spatial profile result in a redistribution of Fourier coefficients in Eq. (5) that represent the momentum state populations. This effect was confirmed using numerical simulations. Since the weighting coefficients are free parameters in the fits, coherence functions can be used to measure momentum state populations associated with a perturbation pulse directly and accurately.

C. Measurement of momentum state populations

In experiments using Bose-condensed gases, the momentum state populations following interaction with a standing-
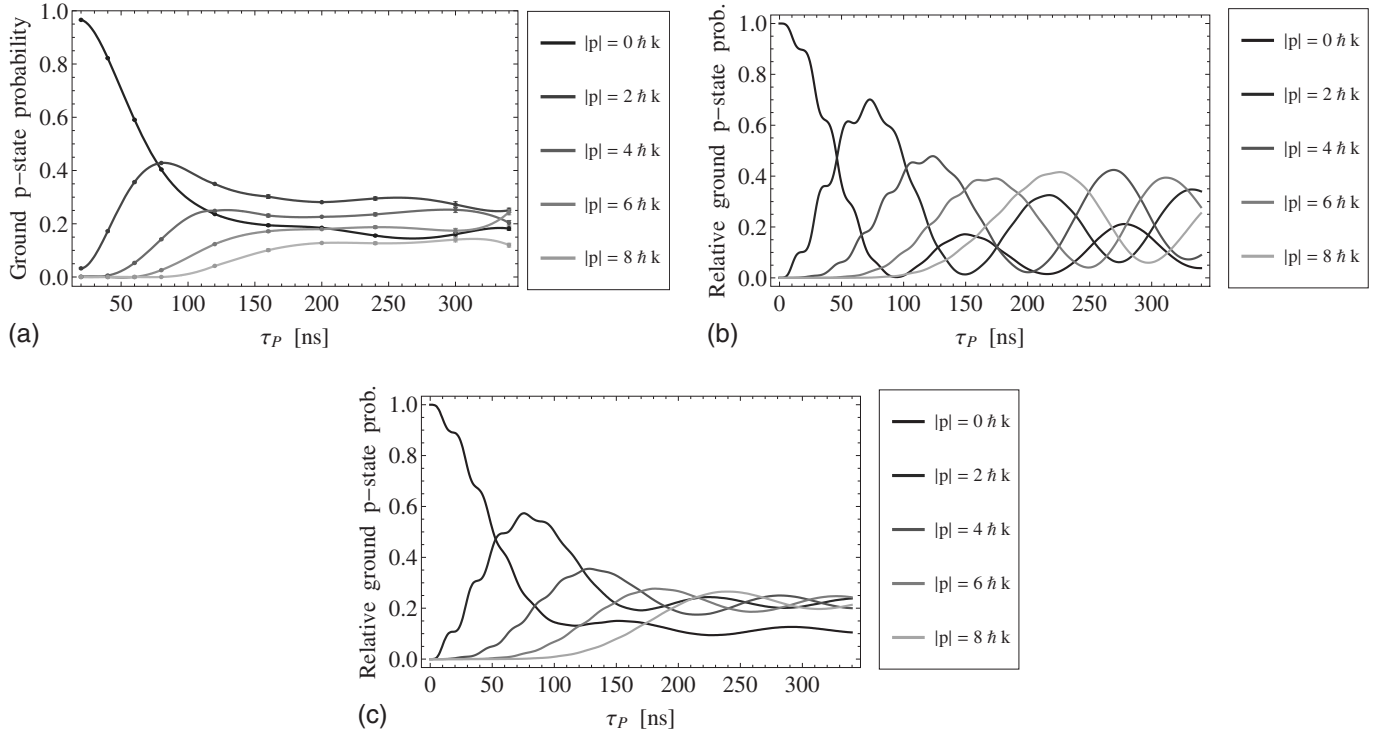
FIG. 10. (a) Probabilities of momentum states associated with the ground state versus τ_p; probabilities extracted from fits using Eq. (5), $\Delta=39.4$ MHz and $\Omega \sim 19.6$ MHz. Here, the probability of $|p|=2n\hbar k$ is plotted as $|\alpha_n|^2+|\alpha_{-n}|^2$ for $n \neq 0$ and $|\alpha_0|^2$ for $n=0$. The points are joined using a fifth-order interpolation function to guide the eyes. (b) MCWF simulations neglecting the effects of spontaneous emission and spatial profile showing probabilities versus τ_p; $\Delta=39.4$ MHz and $\Omega=19.6$ MHz. (c) MCWF simulations including the effects of spontaneous emission and spatial profile for the same conditions as in (b).

wave pulse can be easily inferred from CCD images of the diffracted wave packets [29,39] because the velocity distribution of the sample is much smaller than v_r. In contrast, the echo experiment described here uses laser-cooled samples with a velocity distribution that is much larger than v_r, making direct measurements more challenging.

Figure 10(a) shows the measured populations as a function of τ_p. For each value of τ_p, the populations are determined from the weighting terms, c_n, of the Fourier coefficients of Eq. (5). It is notable that the uncertainties of these coefficients are at the level of a few percent. The data shows the expected decrease in probability of the $n=0$ momentum state and the increase in the probability of higher momentum states as a function of τ_p. Figures 10(b) and 10(c) show the results of numerical simulations that correspond to experimental conditions.

The numerical simulations are based on a one-dimensional Monte Carlo wave-function (MCWF) technique [40] that evolves a time-dependent wave function of a two-level atom using a non-Hermitian Hamiltonian. In this case, the Hamiltonian is associated with a far-detuned standing wave so that

$$\mathcal{H} = \frac{p^2}{2M} + \hbar\Omega \cos(kz)(S^+ + S^-) - \hbar(\Delta + i\Gamma/2)S^+S^-,$$

(27)

where z and p are the position and momentum of the atom, respectively, k is the wave vector of the light, Ω is the Rabi

frequency, and Γ is the spontaneous emission rate associated with the excited state. $S^+ \equiv |e\rangle\langle g|$ and $S^- \equiv |g\rangle\langle e|$ are raising and lowering operators, respectively, for the two-level atom with ground state $|g\rangle$ and excited state $|e\rangle$. The wave function is written as a superposition of momentum states

$$|\psi(t)\rangle = \sum_n \alpha_n(t)|g, p_g^{(n)}\rangle$$
$$= p_0 + 2n\hbar k\rangle + \beta_n(t)|e, p_e^{(n)}\rangle$$
$$= p_0 + (2n+1)\hbar k\rangle,$$

(28)

where p_0 is the initial momentum of the atom and $|\alpha_n(t)|^2$ and $|\beta_n(t)|^2$ are the time-dependent probabilities (populations) of each momentum state. Using the MCWF method of Ref. [40], the problem of evolving the wave function under the influence of the Hamiltonian in Eq. (27) reduces to solving the tridiagonal system of differential equations:

$$\dot{\alpha}_n = -i\frac{[p_g^{(n)}]^2}{2\hbar M}\alpha_n - i\frac{\Omega}{2}(\beta_{n-1} + \beta_n),$$

(29a)

$$\dot{\beta}_n = -\left[i\frac{[p_e^{(n)}]^2}{2\hbar M} + \frac{\Gamma}{2} - i\Delta\right]\beta_n - i\frac{\Omega}{2}(\alpha_n + \alpha_{n+1}).$$

(29b)

We plot the ground state probabilities $|\alpha_n|^2$ as a function of interaction time (perturbation pulse duration, τ_p) for values of $|n|=0$, 1, 2, 3, and 4 with momenta $2n\hbar k$ in Fig. 10(b). For typical experimental conditions, the probability of being in

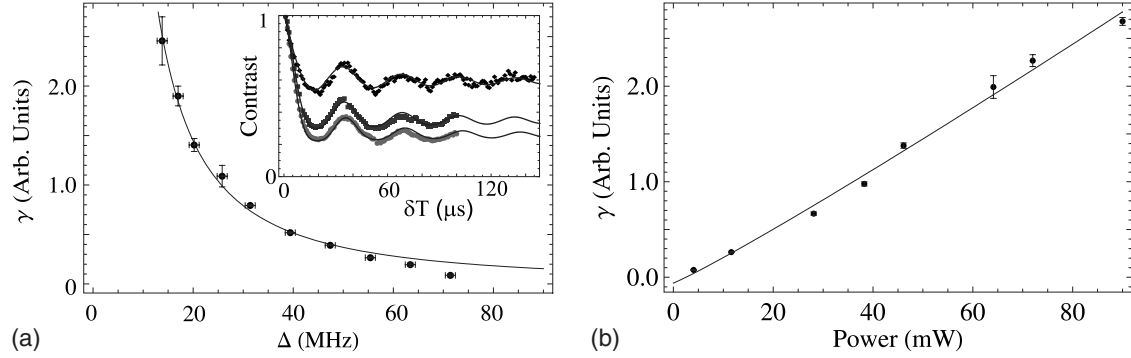FIG. 11. (a) Inset shows contrast versus δT for a traveling-wave perturbation pulse. The body of (a) shows the photon scattering rate, γ, as a function of Δ for $\tau_p = 300$ ns. The data are fit to $\gamma = A \times \Delta^{-p}$, giving $A = 130 \pm 20$ and $p = 1.5 \pm 0.1$. (b) γ versus perturbation pulse power, P, for $\Delta = 50$ MHz. The data are fit to $\gamma = A \times P^{\eta}$, giving $A = 0.022 \pm 0.005$ and $\eta = 1.07 \pm 0.06$.

the excited state is small. Therefore, we neglect the probabilities of momentum states associated with the excited state and normalize the probabilities of momentum states associated with the ground state such that $\sum_{n=-4}^{n=4} |\alpha_n|^2 = 1$. Figure 10(c) shows results of a simulation including the effects of spontaneous emission and the intensity profile of the laser beam that shows good qualitative agreement with the data. The spatial profile of the laser beam is taken into account by averaging the results of simulations carried out using different Rabi frequencies. By allowing Ω to vary along the radial direction as given by $\Omega(r) = \Omega_0 e^{-(r/w)^2}$, where w is the radius of the beam, the results of simulations for different values of r can be combined in a weighted sum. The weights are based on the density profile of the trapped sample.

The application of coherence functions to model such measurements and extract momentum state populations is substantially different from previous methods. In Ref. [10] the grating contrast was measured as a function of T as shown in Fig. 1(b). In this case, the momentum state populations could be inferred from the pulse area determined from a fit to the signal amplitude. This is because the amplitude can be expressed as $J_2[\phi_2 \sin(\omega_r T)]$ in the absence of spontaneous emission and spatial profile effects making it possible to obtain ϕ_2 from a fit. The probability of a particular momentum state $2n\hbar k$ after excitation by a standing-wave pulse can be determined from a knowledge of ϕ_2 since it is given by $J_n^2(\phi_2)$. The signal dependence on T is much more complex in the presence of spontaneous emission and spatial profile effects making it difficult to accurately determine ϕ_2 from a fit. As shown in Fig. 14 in Ref. [10], even a direct knowledge of pulse parameters such as intensity and duration is not sufficient to predict the probability of momentum state populations because atoms sample a range of pulse areas due to the variations in intensity across the sample.

D. Traveling-wave experiments

In Ref. [11] it was established that coherence functions previously used in atomic beam experiments [22–25] could also be applied to model the effects of a traveling-wave perturbation pulse on the grating contrast. In this section, we present a determination of the average number of scattered photons which is similar to the measurements in [23,24] and

additional analysis that allows measurements of scaling laws for the photon scattering rate.

The inset in Fig. 11(a) shows the effect of an far-detuned circularly polarized traveling-wave perturbation pulse on the grating contrast as a function of δT. The time between the AI echo pulses is fixed at $T \sim 1.6$ ms. The contrast shows the expected quasiperiodic modulation at $\sim \omega_r$ and decays to a steady-state value. In comparison with perturbation by a standing-wave pulse, the loss of contrast is associated with decoherence due to spontaneous emission. Each curve in the inset represents data obtained for a particular value of Δ and fixed τ_p.

For all curves in the inset, the fit function is based on Eq. (4) and is qualitatively similar to the signal shape shown in Fig. 2(b). Here, the coefficients c_n give the probability of scattering n photons. These coefficients depend on perturbation pulse parameters such as intensity, detuning, and duration and can be measured to a few percent. The inset of Fig. 11(a) also shows that spontaneous emission reduces the asymptotic value of the contrast if δT is increased. Since the perturbation pulses were off-resonance, the average number of scattered photons per atom, $\bar{n}$, obtained from each data set is generally small ($\bar{n} = 1.5$) and therefore the loss in contrast does not approach 100%. Separate data sets also established that the loss in contrast increases with τ_p.

The steady-state value of each curve in the inset is proportional to c_0 which represents the number of atoms that have not scattered any photons from the perturbation pulse. c_0 can be modeled by the expression $c_0 \propto e^{-\gamma(\Delta)\tau_p}$, where γ is the detuning-dependent photon scattering rate. The body of Fig. 11(a) shows the negative natural logarithm of c_0 as a function of Δ. For each value of Δ, c_0 is determined from the ratio of the contrast with and without the perturbation pulse for $\delta T \gg T_r$. A fit to the data shows a power-law dependence of γ on Δ that can be described by $\gamma \propto \Delta^{-p}$. The fit gives a value of $p = 1.5 \pm 0.1$ which is reasonable considering that the pulse intensity was substantial ($I \sim 10 I_{sat}$). In comparison, for the weak field off-resonant case simulations based on [41] suggest that γ is expected to show an inverse squared dependence on Δ ($p = 2$). Figure 11(b) shows the dependence of γ on the perturbation pulse power. Again, γ was determined from measurements of c_0 with $\delta T \gg T_r$. The data confirms the expected linear dependence for the scattering rate.

E. cw scattering experiments

We have also explored the loss of contrast due to weak cw traveling-wave background light. In the presence of cw light during the experiment, the contrast is expected to decrease monotonically due to random scattering events. This should result in an exponential decrease in contrast as a function of T. The time scale over which the momentum states decohere is of the order of T_r since $\sim \frac{\lambda/2}{\hbar k/m}$ represents the time in which wave packets move a distance of the order of the grating spacing due to photon scattering.

Figure 12(a) shows the echo amplitude as a function of T for various intensities of circularly polarized cw light. In Ref. [11], the photon scattering cross section was obtained from this data. The cross section was found to be consistent with the expected value of $3\lambda^2/2\pi$ and independent of T. This is consistent with the idea that photon scattering imparts a velocity change in at least $\hbar k/m$ (1.2 cm/s) that decoheres the signal on a time scale of $\sim 1/\omega_r$.

In this paper, we model the signal decay in Fig. 12(a) as a product of a Gaussian component (that represents the time of flight of atoms from the region of interaction) and an exponential component (that represents decoherence due to photon scattering). The fit parameters associated with the Gaussian component remain unchanged as the intensity of the cw light is varied. Figures 12(b) and 12(c) show the exponential decay constant, which is the photon scattering rate, plotted as a function of detuning and intensity of cw light, respectively. The scattering rate scales linearly with intensity and as the inverse square of the detuning, trends that are consistent with expectations.

V. CONCLUSIONS

In this work, we present an analytical calculation based on the theory of echo formation that describes periodic revivals in the grating contrast in the presence of standing-wave perturbation pulses. The predictions are in good agreement with the signal shape obtained using the theory of coherence functions. The theory of echo formation predicts scaling laws for the FWHM of the revivals in contrast as a function of perturbation pulse area and the number of pulses. These scaling laws have been investigated and it has been shown that they can be exploited to achieve a significant improvement in the precision of ω_r measured in Ref. [11]. We expect to utilize the technique of perturbation pulses for precise determinations of ω_r which will be carried out by extending the experimental time scale to the transit time limit and by completing a thorough study of systematic effects. A suitably long time scale has recently been achieved by eliminating magnetic field gradients and expanding the size of the excitation beams to several centimeters. As noted in Ref. [11], the expected precision in such a measurement of ω_r is estimated to be ~ 20 ppb on a time scale of ~ 100 ms. We also show that coherence functions can be used for accurate measurements of momentum states populations. Finally, the paper discusses distinctive effects of traveling-wave and cw decoherence that have been used to measure scaling laws for
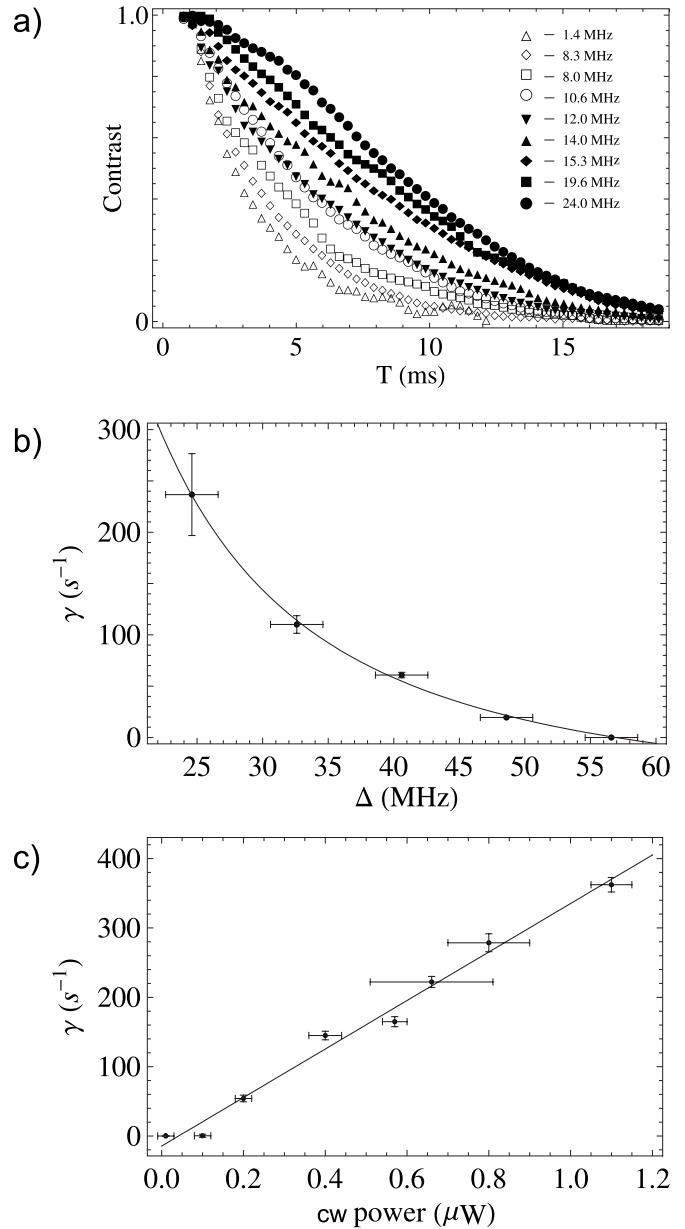

FIG. 12. (a) Contrast as a function of T for variable cw detuning. (b) The exponential decay constant, γ, for the curves in (a) as a function of Δ for fixed cw power of 750 nW; fit to $b + m \times \Delta^{-p}$ gives $p = 1.9 \pm 0.3$. (c) γ versus cw power, P, for $\Delta = 46$ MHz; fit to $A \times P^\eta$ gives $A = 340 \pm 10$ s^{-1}/μW and $\eta = 1.08 \pm 0.09$.

the photon scattering rate. These trends are consistent with expectations.

[1] D. S. Weiss, B. C. Young, and S. Chu, Phys. Rev. Lett. **70**, 2706 (1993).

[2] A. Wicht, J. M. Hensley, E. Sarajlic, and S. Chu, Phys. Scr., T **T102**, 82 (2002).

[3] P. Cladé, E. de Mirandes, M. Cadoret, S. Guellati-Khélifa, C. Schwob, F. Nez, L. Julien, and F. Biraben, Phys. Rev. Lett. **96**, 033001 (2006).

[4] M. Cadoret, E. de Mirandes, P. Cladé, S. Guellati-Khélifa, C. Schwob, F. Nez, L. Julien, and F. Biraben, Phys. Rev. Lett. **101**, 230801 (2008).

[5] S. B. Cahn, A. Kumarakrishnan, U. Shim, T. Sleator, P. R. Berman, and B. Dubetsky, Phys. Rev. Lett. **79**, 784 (1997).

[6] S. Gupta, K. Dieckmann, Z. Hadzibabic, and D. E. Pritchard, Phys. Rev. Lett. **89**, 140401 (2002).

[7] M. Weel and A. Kumarakrishnan, Phys. Rev. A **67**, 061602(R) (2003).

[8] M. Weel, I. Chan, S. Beattie, A. Kumarakrishnan, D. Gosset, and I. Yavin, Phys. Rev. A **73**, 063624 (2006).

[9] M. Weel, Ph.D. thesis, York University, 2005.

[10] S. Beattie, B. Barrett, M. Weel, I. Chan, C. Mok, S. B. Cahn, and A. Kumarakrishnan, Phys. Rev. A **77**, 013610 (2008).

[11] S. Beattie, B. Barrett, I. Chan, C. Mok, I. Yavin, and A. Kumarakrishnan, Phys. Rev. A **79**, 021605(R) (2009).

[12] D. V. Strekalov, A. Turlapov, A. Kumarakrishnan, and T. Sleator, Phys. Rev. A **66**, 023601 (2002).

[13] P. R. Berman, *Atom Interferometry* (Academic Press, New York, 1997).

[14] M. Berry, I. Marzoli, and W. P. Schleich, Phys. World **14**, 39 (2001).

[15] J. F. Clauser and S. Li, Phys. Rev. A **49**, R2213 (1994).

[16] E. M. Rasel, M. K. Oberthaler, H. Batelaan, J. Schmiedmayer, and A. Zeilinger, Phys. Rev. Lett. **75**, 2633 (1995).

[17] D. M. Giltner, R. W. McGowan, and S. A. Lee, Phys. Rev. Lett. **75**, 2638 (1995).

[18] S. Bernet, M. K. Oberthaler, R. Abfalterer, J. Schmiedmayer, and A. Zeilinger, Phys. Rev. Lett. **77**, 5160 (1996).

[19] P. J. Martin, B. G. Oldaker, A. H. Miklich, and D. E. Pritchard, Phys. Rev. Lett. **60**, 515 (1988).

[20] A. Turlapov, A. Tonyushkin, and T. Sleator, Phys. Rev. A **71**, 043612 (2005).

[21] G. K. Campbell, A. E. Leanhardt, J. Mun, M. Boyd, E. W. Streed, W. Ketterle, and D. E. Pritchard, Phys. Rev. Lett. **94**, 170403 (2005).

[22] T. Pfau, S. Spalter, C. Kurtsiefer, C. R. Ekstrom, and J. Mlynek, Phys. Rev. Lett. **73**, 1223 (1994).

[23] M. S. Chapman, T. D. Hammond, A. Lenef, J. Schmiedmayer, R. A. Rubenstein, E. Smith, and D. E. Pritchard, Phys. Rev. Lett. **75**, 3783 (1995).

[24] D. A. Kokorowski, A. D. Cronin, T. D. Roberts, and D. E. Pritchard, Phys. Rev. Lett. **86**, 2191 (2001).

[25] H. Uys, J. D. Perreault, and A. D. Cronin, Phys. Rev. Lett. **95**, 150403 (2005).

[26] L. Mandel, J. Opt. (Paris) **10**, 51 (1979).

[27] F. L. Moore, J. C. Robinson, C. F. Bharucha, B. Sundaram, and M. G. Raizen, Phys. Rev. Lett. **75**, 4598 (1995).

[28] S. Wimberger and A. Buchleitner, J. Phys. B **39**, L145 (2006).

[29] C. Ryu, M. F. Andersen, A. Vaziri, M. B. d'Arcy, J. M. Grossman, K. Helmerson, and W. D. Phillips, Phys. Rev. Lett. **96**, 160403 (2006).

[30] S. Wimberger, R. Mannella, O. Morsch, and E. Arimondo, Phys. Rev. Lett. **94**, 130404 (2005).

[31] M. F. Andersen, A. Kaplan, T. Grunzweig, and N. Davidson, Phys. Rev. Lett. **97**, 104102 (2006).

[32] A. Tonyushkin, S. Wu, and M. Prentiss, Phys. Rev. A **79**, 051402(R) (2009).

[33] S. Wu, A. Tonyushkin, and M. Prentiss, Phys. Rev. Lett. **103**, 034101 (2009).

[34] W. H. Oskay, D. A. Steck, V. Milner, B. G. Klappauf, and M. G. Raizen, Opt. Commun. **179**, 137 (2000).

[35] M. B. d'Arcy, R. M. Godun, M. K. Oberthaler, D. Cassettari, and G. S. Summy, Phys. Rev. Lett. **87**, 074102 (2001).

[36] R. Feynman, *The Feynman Lectures* (Addison-Wesley, Reading, MA, 1963).

[37] M. Weitz, T. Heupel, and T. W. Hänsch, Phys. Rev. Lett. **77**, 2356 (1996).

[38] A. Vorozcovs, M. Weel, S. Beattie, S. Cauchi, and A. Kumarakrishnan, J. Opt. Soc. Am B **22**, 943 (2005).

[39] L. Deng, E. W. Hagley, J. Denschlag, J. E. Simsarian, M. Edwards, C. W. Clark, K. Helmerson, S. L. Rolston, and W. D. Phillips, Phys. Rev. Lett. **83**, 5407 (1999).

[40] K. Mølmer, Y. Castin, and J. Dalibard, J. Opt. Soc. Am. B **10**, 524 (1993).

[41] L. Allen and J. H. Eberly, *Optical Resonance and Two-Level Atoms* (Dover, New York, 1987).